

3D printed protein-based robotic structures actuated by molecular motor-based cortices

Haiyang Jia

<https://orcid.org/0000-0002-8330-5031>

Johannes Flommersfeld

Ludwig-Maximilians-Universität München

Michael Heymann

University Stuttgart <https://orcid.org/0000-0002-9278-8207>

Sven Vogel

Max Planck Institute of Biochemistry

Henri Franquelim

MPI of Biochemistry <https://orcid.org/0000-0001-6229-4276>

David Brueckner

Ludwig-Maximilians-Universität München

Hirumune Eto

Max Planck Institute of Biochemistry

Chase Broedersz

Ludwig Maximilian University of Munich <https://orcid.org/0000-0001-7283-3704>

Petra Schwille (✉ schwille@biochem.mpg.de)

Max Planck Institute of Biochemistry <https://orcid.org/0000-0002-6106-4847>

Article

Keywords: motor protein activity, 3D printing, molecular motor-based cortices

Posted Date: September 15th, 2021

DOI: <https://doi.org/10.21203/rs.3.rs-863696/v1>

License:   This work is licensed under a Creative Commons Attribution 4.0 International License.

[Read Full License](#)

Version of Record: A version of this preprint was published at Nature Materials on May 26th, 2022. See the published version at <https://doi.org/10.1038/s41563-022-01258-6>.

Abstract

Upscaling motor protein activity to perform work in man-made devices has long been an ambitious goal in bio-nanotechnology. The use of hierarchical motor assemblies, as realized in sarcomeres, has so far been complicated by the challenges of arranging sufficiently high numbers of motor proteins with nanoscopic precision. Here we suggest an alternative approach based on actomyosin cortex-like force production, allowing low complexity motor arrangements in a contractile meshwork that can be locally activated by ATP. The design is reminiscent of a motorized exoskeleton coating and thereby actuating soft protein-based polymer structures from the outside. This readily supports the connection and assembly of micro-3D printed modules into larger structures, thereby scaling up mechanical work. We provide an analytical model of force production in these systems and demonstrate the design flexibility by 3D printed units performing complex mechanical tasks, such as micro-arms and hands that perform sign language and wave.

Main Text

Living systems are a source of inspiration for man-made robotics¹⁻³ with regard to flexibility, scalability, and resilience. Recent progress in micro-3D printing and synthetic biology⁴ raises expectations that a bottom-up design of nano- to microscale biorobots^{5,6} directly from the level of biomolecules may become reality. While the design and fabrication of soft biomimetic robots has become increasingly successful over the past decades, a major remaining challenge for potential use in or on living systems is their biocompatible actuation. Cellular motor proteins⁷⁻¹¹, which directly turn metabolic energy into mechanical work, represent promising candidates from nature to execute mechanical operations on soft materials¹². In contrast to electromechanical and biohybrid actuators¹³⁻¹⁷, which require considerable efforts for downscaling to the nano/microscale³, a key challenge for utilizing molecular motors is to upscale force and work to operate devices that are many orders of magnitude larger¹⁸⁻²¹. Efficient large-scale use of such protein motor systems for actuation of soft robots has so far been mainly realized through cyborg constructions hybridizing living muscle cells and tissue with soft polymer materials such as silicone^{13,14,22}. Recently, a large-scale kinesin motor-based network has been successfully engineered to actuate established soft microstructures²³; the actuators were, however, untethered and had to be recruited specifically from the environment. Coupling the protein motors to soft materials has still been complicated by the challenges of producing biomimetic templates that are both sufficiently malleable and physiologically compatible with the large-scale operation of motor protein systems.

We here introduce shape-morphing protein-based robotic structures composed of programmable 3D printed modular units^{24,25} (Fig. 1a), which can be actuated by a minimal artificial actomyosin exoskeleton. This motorized exoskeleton can be viewed as a scaled-up actomyosin cortical layer²⁶ connecting the different parts of the deformable robotic structure (Fig. 1b). Our exoskeleton design harnesses the contractility generated by myosin molecular motors and transduces the resulting active stresses to perform large-scale mechanical work on the 3D soft device, without the need of hierarchically

structured motor assemblies as in sarcomeres. To characterize force production by the contractions of actomyosin layers and the resulting deformation of soft frames, we designed contractile pillar ring modules of different sizes and stiffnesses. The simple geometry of this design allows us to develop a theoretical model to conceptually understand contraction dynamics and demonstrate stiffness-insensitive force generation. We then apply our approach to more complex shape-morphing structures, by combining basic modules, such as pillars, panels, and hinges, thereby mimicking key elements of human hands (Fig. 1c). Finally, we show that the exoskeleton design can be extended and scaled up to realize complex programmable shape transformations of active mechanical devices, and further achieve multi-stage functions of soft robotic elements with (selectively) light-activatable modules (Fig. 1d).

To quantitatively understand the basic performance of our contractile motorized exoskeleton with regard to force generation and transduction in shape-morphing of 3D protein-based modules, we first designed a simple structure consisting of a ring of ten soft pillars (Fig. 2a, Extended Data Fig. 1a-b). The hydrogel pillar units are printed by two-photon polymerization of bio-resin consisting of bovine serum albumin (BSA) and rose bengal as photoinitiator. The Young's modulus of the protein hydrogel can be tuned from 10 kPa to 250 kPa (Extended Data Fig. 2), corresponding to moduli of biological tissues^{27,28}. Subsequently, the ring structure is biotinylated and decorated by an F-actin meshwork via biotin-actin and neutravidin coupling. The actin filaments are further cross-linked by neutravidin to enhance the network's mechanical integrity (Fig. 2b, Extended Data Fig. 3-4). To complete the exoskeleton-like minimal actomyosin cortex, pre-assembled myofilaments with skeletal muscle myosin II were included. Upon ATP addition these myosin motors generate contractile forces^{26,29} that are transduced by the exoskeleton resulting in large-scale active stresses that drive the inward deflection of the pillar ring (Fig. 2, Movie S1).

Next, we investigated how the contractile performance of the 3D structures depends on their dimensions by varying the diameter D of the pillar ring. The diameter can be enlarged by increasing the interpillar distance d and maintaining a constant pillar number N ($N=10$), or by increasing N and keeping d constant ($d=5\ \mu\text{m}$) (Fig. 2c-d, Extended Data Fig. 5). We noticed that the deflections of pillars towards the centre were determined by the density and integrity of the actin mesh located inside the ring (Fig. 2c-d). Rings with larger diameters develop holes in the actomyosin meshwork, resulting in asymmetric and incoherent contraction of the ring as a whole (Fig. 2d). This effect is exacerbated by larger interpillar distance (Fig. 2d left, Extended Data Fig. 5c-e). In contrast, increasing the pillar numbers at similar diameters ($D=26\ \mu\text{m}$) results in significantly higher network density (Fig. 2c), better preserving the integrity of the networks. However, isotropic contractions are rarely observed for pillar rings with diameters $\geq 30\ \mu\text{m}$ (Fig. 2d). These insights lead us to a key design feature with regard to the scale over which the exoskeleton scaffold can achieve effective and coherent contractions, suggesting that concatenating smaller force-transducing modules can be a good option to engineer larger device designs.

Another design feature for robotics engineering is to combine modules with different mechanical properties and programmable macroscopic deformations³⁰. To explore the effect of elasticity on the contraction capacity of the actomyosin exoskeleton, we varied the stiffness of the pillars in the pillar-ring test assay, while keeping the density of the meshwork constant (Fig. 2e-f, Extended Data Fig. 6). We

found that the pillar deformations can be tuned by varying the material stiffnesses. The largest pillar deflection was observed in rings with a Young's modulus of 57 ± 12 kPa (Extended Data Fig. 2f). In this case, the contractile exoskeleton is able to reduce its radial dimension by up to a factor 0.5, resulting in large pillar strains up to 0.3 (Fig. 2e). Importantly, the pillar ring design allows us to quantify the forces generated by the active contraction. By comparing the measured pillar deflection profiles with Euler beam theory³¹ (Fig. 2f, SI-Sec. 1), we measure active forces generated by the actomyosin exoskeleton of 126 ± 22 pN ($n=12$) per pillar upon full contraction. Individual myosin filaments under these conditions can generate forces close to 20-60 pN^{26,32,33}, suggesting that only a small fraction of the estimated (mean \pm s.d.; $n=9$) myofilaments (Supplementary Fig. S1) in the exoskeleton effectively contribute to the contraction (SI-Sec. 2). However, the force generation in the system can be tuned by varying the density of the actin network coated on to the 3D scaffolds, by either changing the amount of anchor points (Extended Data Fig. 3c-d, Extended Data Fig. 7c-d) or by varying crosslinker concentrations (Extended Data Fig. 4e-g). For a given actin density, however, the force generation is robust over a wide range of pillar stiffnesses (Fig. 2g). The insensitivity of the contractile forces to the frame stiffness facilitates the predictability of force generation in more complex structures, which consist of modules with different stiffnesses.

To understand the build-up of these generated forces, we next investigated the contraction dynamics of actomyosin networks on the microstructures. Upon myosin activation, the pillars start to bend inwards (Fig. 2h). The contraction velocity initially increases markedly over the course of approximately one minute, followed by a decelerating contraction towards a final state (Fig. 2i). The maximal velocity that is reached during the contraction depends sensitively on pillar stiffness (Fig. 2j, Extended Data Fig. 7, Movie S1). We observed a clear increase in peak velocity with decreasing pillar stiffness below a value of ≈ 100 pN/ μ m. Interestingly, the acceleration lasts much longer than the dynamics of single or spatiotemporally coordinated myosin motors in sarcomeres, which operate on the timescale of milliseconds³⁴.

To elucidate the mechanisms that are underlying the observed robust force generation and the dynamics of the contraction, we describe our contractile system by a simple, one-dimensional analytical model. In this viscoelastic model the pillar's and the network's elastic response is represented by elastic springs and the viscous response of the network is characterized by a dashpot. The myosin activity is modelled by a time-dependent contractile force, acting on the pillars (Fig. 2a, details in SI). To capture the contraction dynamics, we include a microscopic description of force generation by the molecular motors: myosin filaments transiently bind to the F-actin network where they contribute to contractile force generation. These myosin binding dynamics, and the resulting force generation, thus depend on the number of myosin filaments and the density of actin in the gel³⁵. Finally, we find that it is essential to account for the known load-dependence of the myosin binding dynamics³⁶ (SI-Sec. 3.4). As the force builds up, the load-dependent myosin kinetics results in an increased number of motors being engaged in force generation.

The inherent positive feedback between the slow build-up of viscoelastic network stresses and the active force generation by fast load-dependent myosin binding kinetics in our model gives rise to the intricate contraction dynamics of the pillar-ring, in quantitative agreement with our experiments (Fig. 2i). When possible, the parameters of our dynamic 1D contractility model are chosen based on literature values (see table S1). The remaining parameters are fully constrained by fitting the model to a single contraction curve at one pillar stiffness (Fig. 2i). This model accurately predicts the dynamics and steady-state values of the actively generated forces over broad range of pillar stiffness (steady state: Fig. 2e-g, Extended Data Fig. 6), including the stiffness-dependence of the contraction velocities (Fig. 2j). The stiffness-insensitivity of the steady-state force can be explained by our contractility model (Fig. 2g, solid line), provided that the network's elastic response is much softer than the pillar stiffness and can thus be neglected (SI-Sec. 3.1). Conceptually, the load-sensitivity of the myosin binding kinetics results in active force generation, which is largely controlled by the internal stress of the actin network and is insensitive to the stiffness of the frame. In contrast, when only accounting for an actin density-dependent contractility as in other models³⁵, the stiffness dependence was predicted incorrectly (Fig. 2g, dash line, SI-Sec. 3.3). Finally, using our 1D contractility model together with the experiments, we can also estimate that generated mechanical power of the exoskeleton in the pillar-ring assay peaks for 43×10^{-18} W (SI-Sec. 3.5).

Having gained conceptual understanding of the force generation and contraction dynamics of the actomyosin exoskeleton on soft-frames with simple geometries, we next turn to applications involving complex 3D structures with programmable transformations. The central idea is to assemble 3D structures from modules with tunable stiffnesses to perform controllable deformations. A key structural element to advance complexity to the next level is a hinge module. Thus, we designed a V-shaped hinge with two stiff arms (pillars) connected by a soft joint (thickness ratio $_{\text{arm/joint}}$: 4:1) and a stabilizing apex to inhibit overstretching to angles beyond 180° (Fig. 3a, Extended Data Fig. 1c). Upon myosin activation, the hinge is actuated, i.e., the free arm rotates about the soft joint towards the fixed arm, which follows the dynamic behaviours of pillar rings and exhibits with an initial acceleration phase and a deceleration phase (Movie S2, Extended Data Fig. 8). The active closure of V-units can be accomplished for a range of convex angles, e.g. from 45° to 160° (Fig. 3b), and can be tuned by the fabrication parameters (Extended Data Fig. 8).

Further, to explore the possibilities for reversible operation of our protein hydrogel devices, we designed an alternative round joint V-unit with homogeneous elasticity (Supplementary Fig. S2). Since the activity of myosin motors is sensitive to the ATP concentration, the reversible shape transformation can be implemented by switching between high and low ATP conditions (Fig. 3c, Movie S3). Low concentration ATP (0.5 mM) can initiate the active closure of the hinge, as demonstrated above. In contrast, high concentrations of ATP (4 mM) cause myofilaments to detach from the actin exoskeleton, resulting in a relaxation of the elastic hydrogel structures. We successfully performed two repeats of contraction by manually exchanging the ATP concentrations (Fig. 3c). After the second iteration, the structures started to lose their reversibility in response to high ATP concentration. The robust reversibility is partially hampered

by the non-reversible breakage and crosslinking of actin networks^{26,29}. We also noticed softer structures showed larger displacements, but exhibit lower reversibility, due to larger energy dissipation³⁷. Thus, structures with different rigidity exhibit an opposite trend between displacement and reversibility (Fig. 3d). To engineer a reversible shape change, we seek an optimal tradeoff between these factors.

Scaling up the mechanical work performed by our actomyosin-actuated protein-based robots can now be achieved by concatenating active modules to engineer larger structures. For example, by concatenating the V-units, large modular architectures can be assembled, as illustrated in Fig. 4a. Specifically, V-units were combined into a zigzag module and the connection sites between V-units were stabilized to permit folding only on the bottom joints. The actomyosin actuators then independently trigger the closure of all V-units, resulting in a rapid curling of the zigzag module (Movie S4). Instead of using one large hinge angle, 90° and 135° angle folding can be accomplished by combining two or three 45° V-units, respectively (Extended Data Fig. 9a). Similarly, large angles that are impossible to achieve with a single unit, such as 180° and 360°, can also be successfully accomplished by concatenating modules. The spring-like zigzag module combined with six V-units could revolve around the first joint on the right, circularly coiling up its long V-chain and finally forming a closed hexagonal star (Fig. 4b). Besides the curling-up, a hydrogel spring-shape structure with additional degrees of freedom can contract along its axis upon myosin-triggered actuation (Extended Data Fig. 9b-e). These examples demonstrate the versatility and potential upscaling of programmable mechanical operations that can be achieved³⁷ in our protein-based active robotics.

Another desired feature of active biomimetic devices is the ability to fold 2D surfaces into complex 3D shapes. To accomplish this, we expanded our approach to generate a more intricate shape-morphing, such as the self-folding of a hydrogel cube from a cruciform precursor consisting of six hinged panels (Fig. 4c-d, Extended Data Fig. 1d). The solid-supported central face was connected to the other five free-standing faces with inner hinges. An extra rigid block was placed between the two hinging faces to serve as a sill for controlling the folding angle. The flat panels and the rigid block formed a 90° angle, which enabled a simple 2D self-folding sheet to yield a 3D cube under active contraction (Movie S5).

To further extend the functional complexity of our protein-based robotics, we created programmable and reversible microscale robots with light-induced spatiotemporal control. First, we employed the bio-actuated 3D protein hydrogel to mimic grasping micro-hands consisting of a panel with five attached fingers (Fig. 4e). The connections between phalanges and the palm were mediated with soft joints. In our designs, the actomyosin exoskeleton functions as an external “muscle” layer to actuate the five fingers with respect to the palm into a grasping shape (Extended Data Fig. 9f, Movie S6). By selectively constraining the finger joints kinematically with triangular-shaped blocker modules (wedges), we programmed anthropomorphic gestures, like “OK” (Extended Data Fig. 9f). Sign language that is even more complicated can be executed successfully within minutes, such as **I Love You (ILY)** (Fig. 4f).

Finally, we combined the micro-hand and the chain of V-units into a miniature robotic arm - fully made from and actuated by proteins (Fig. 4g-h, Movie S7). Initiating the contraction of the external actomyosin

exoskeleton triggered the arm into a raising and grasping motion. As a first proof of concept of reversible operation, the artificial arm was subjected to a high-ATP condition (4mM ATP) and responded with a twitch (Movie S7). We next explored how artificial arm motions could be designed as goal-directed behaviors subject to multistage control. Using photocaged (NPE-caged) ATP as molecular light sensor, the ATP-dependent actuation module, i.e. the actomyosin exoskeleton on the surface of the robotic arm, can be remotely controlled with light (Fig. 4i, Extended Data Fig. 10). Through spatiotemporally targeted release of ATP by illumination with a focused 405 nm diode laser, stepwise arm and hand movements can be guided by light stimuli within one minute (Fig. 4i, Movie S8). Due to the photo damage, the light activation can only be used for single-run applications. Interestingly, as expected based on our model, the complex structure activated by light and preloaded motors can respond more rapidly than by recruiting motors and energy out of solutions, suggesting a new avenue for improving the performance of our system in the future.

To conclude, we demonstrate the ability of 3D printing complex protein-based microrobotics functionalized with a minimal actomyosin exoskeleton as its actuating system. Hereby, the efficient and scalable operation of reconstituted biological motor assemblies as contractile layers enabled the large-scale shape-morphing of complex 3D microstructures by converting chemical energy directly into mechanical work. Furthermore, being designed and assembled entirely from biomolecules in a bottom-up fashion, the self-powered soft robotic system constitutes an excellent starting point as a chassis. The performance in terms of speed, force, and reversibility, may in the future be advanced by operating under automated microfluidics², by optimizing actomyosin network composition³⁸ with natural crosslinking proteins³⁹, and by integrating other biological or biomimetic modules^{11,40}, such as actin recycling systems⁴¹. We consider this an exciting step in engineering and programming arbitrarily shaped bio-motor-based actuators for future soft robotics¹, which no longer rely on the swelling and shrinking of materials. In the framework of the bottom-up assembly of life-like systems, as pursued by us and others^{1,4,13}, the technology we developed here opens new vistas for various applications, such as custom-shaped dynamic sensors and bioassays, microrobots for *in vivo* biomedical tasks, and proto-tissue engineering, when introduced to the life sciences^{42,43}.

Declarations

Acknowledgements: We thank F. Siedler for help in SEM characterizations. We acknowledge funding from GRK2062, SFB863, EXC-2094 and SFB 1032 funded by Deutsche Forschungsgemeinschaft (DFG), the MaxSynBio consortium funded by the Federal Ministry of Education and Research of Germany and the Max Planck Society.

Author contributions: H.J., M.H., S.K.V. and P.S. conceived and initiated the project; H.J. contributed to experimental design, planning, and execution; S.K.V contributed to the actomyosin system; M.H. and H.E. helped for 3D printing and design; J. F., D.B.B. and C.P.B. contributed to the theoretical model; H.J., J.F.

and H.G.F. contributed to data analysis. All the authors contributed interpretation. H.J., P.S., J.F., D.B.B. and C.P.B. wrote the paper with help of other authors.

Competing interests: The authors declare no conflict of interest.

Additional information

Extended data Fig. 1-Fig. 10

Supplementary information

Movies S1 to S8

Data Availability

All data generated or analyzed during this study are included in the published article and its Supplementary Information, and are available from the corresponding author on reasonable request.

Code availability

The codes for 3D printing and simulation are available upon request.

References

1. Rus, D. & Tolley, M. T. Design, fabrication and control of soft robots. *Nature* **521**, 467–475 (2015).
2. Rich, S. I., Wood, R. J. & Majidi, C. Untethered soft robotics. *Nat. Electron.* **1**, 102–112 (2018).
3. Yang, G.-Z. *et al.* The grand challenges of Science Robotics. *Sci. robot.* **3**, eaar7650 (2018).
4. Jia, H. & Schwille, P. Bottom-up synthetic biology: reconstitution in space and time. *Curr. Opin. Biotechnol.* **60**, 179–187 (2019).
5. Cianchetti, M., Laschi, C., Menciassi, A. & Dario, P. Biomedical applications of soft robotics. *Nat. Rev. Mater.* **3**, 143–153 (2018).
6. Sitti, M. Miniature soft robots—road to the clinic. *Nat. Rev. Mater.* **3**, 74 (2018).
7. Nédélec, F., Surrey, T., Maggs, A. C. & Leibler, S. Self-organization of microtubules and motors. *Nature* **389**, 305 (1997).
8. Sanchez, T., Chen, D. T., DeCamp, S. J., Heymann, M. & Dogic, Z. Spontaneous motion in hierarchically assembled active matter. *Nature* **491**, 431 (2012).
9. Le Goff, L., Amblard, F. & Furst, E. M. Motor-driven dynamics in actin-myosin networks. *Phys. Rev. Lett.* **88**, 018101 (2001).
10. Humphrey, D., Duggan, C., Saha, D., Smith, D. & Käs, J. Active fluidization of polymer networks through molecular motors. *Nature* **416**, 413 (2002).
11. Fletcher, D. A. & Mullins, R. D. Cell mechanics and the cytoskeleton. *Nature* **463**, 485–492 (2010).

12. Saper, G. & Hess, H. Synthetic systems powered by biological molecular motors. *Chem. Rev.* **120**, 288–309 (2019).
13. Nawroth, J. C. *et al.* A tissue-engineered jellyfish with biomimetic propulsion. *Nat. Biotechnol.* **30**, 792–797 (2012).
14. Park, S.-J. *et al.* Phototactic guidance of a tissue-engineered soft-robotic ray. *Science* **353**, 158–162 (2016).
15. Aydin, O. *et al.* Neuromuscular actuation of biohybrid motile bots. *Proc. Natl. Acad. Sci. U. S. A* **116**, 19841–19847 (2019).
16. Zhang, X., Chan, F. K., Parthasarathy, T. & Gazzola, M. Modeling and simulation of complex dynamic musculoskeletal architectures. *Nat. Commun.* **10**, 1–12 (2019).
17. Raman, R. *et al.* Optogenetic skeletal muscle-powered adaptive biological machines. *Proc. Natl. Acad. Sci. U. S. A* **113**, 3497–3502 (2016).
18. Ronceray, P., Broedersz, C. P. & Lenz, M. Fiber networks amplify active stress. *Proc. Natl. Acad. Sci. U. S. A* **113**, 2827–2832 (2016).
19. Harris, A. R., Jreij, P. & Fletcher, D. A. Mechanotransduction by the actin cytoskeleton: converting mechanical stimuli into biochemical signals. *Annu. Rev. Biophys.* **47**, 617–631 (2018).
20. Bausch, A. & Kroy, K. A bottom-up approach to cell mechanics. *Nat. Phys.* **2** (2006).
21. Kasza, K. E. *et al.* The cell as a material. *Curr. Opin. Biotechnol.* **19**, 101–107 (2007).
22. Guix, M. *et al.* Biohybrid soft robots with self-stimulating skeletons. *Sci. robot.* **6**, eabe7577, doi:10.1126/scirobotics.abe7577 (2021).
23. Nitta, T., Wang, Y., Du, Z., Morishima, K. & Hiratsuka, Y. A printable active network actuator built from an engineered biomolecular motor. *Nat. Mater.*, 1–7 (2021).
24. Kaehr, B. & Shear, J. B. Multiphoton fabrication of chemically responsive protein hydrogels for microactuation. *Proc. Natl. Acad. Sci. U. S. A.* **105**, 8850–8854 (2008).
25. Jia, H. *et al.* Shaping Giant Membrane Vesicles in 3D-Printed Protein Hydrogel Cages. *Small*, 1906259 (2020).
26. Vogel, S. K., Petrasek, Z., Heinemann, F. & Schwille, P. Myosin motors fragment and compact membrane-bound actin filaments. *Elife* **2**, e00116 (2013).
27. Kot, B. C. W., Zhang, Z. J., Lee, A. W. C., Leung, V. Y. F. & Fu, S. N. Elastic modulus of muscle and tendon with shear wave ultrasound elastography: variations with different technical settings. *PLoS one* **7**, e44348 (2012).
28. Mirfakhrai, T., Madden, J. D. & Baughman, R. H. Polymer artificial muscles. *Mater. Today* **10**, 30–38 (2007).
29. e Silva, M. S. *et al.* Active multistage coarsening of actin networks driven by myosin motors. *Proc. Natl. Acad. Sci. U. S. A.* **108**, 9408–9413 (2011).
30. Laschi, C., Mazzolai, B. & Cianchetti, M. Soft robotics: Technologies and systems pushing the boundaries of robot abilities. *Sci. Robot* **1**, eaah3690 (2016).

31. Trichet, L. *et al.* Evidence of a large-scale mechanosensing mechanism for cellular adaptation to substrate stiffness. *Proc. Natl. Acad. Sci. U. S. A.* **109**, 6933–6938 (2012).
32. Kalganov, A. *et al.* Forces measured with micro-fabricated cantilevers during actomyosin interactions produced by filaments containing different myosin isoforms and loop 1 structures. *Biochim. Biophys. Acta* **1830**, 2710–2719 (2013).
33. Cheng, Y.-S., de Souza Leite, F. & Rassier, D. E. The load dependence and the force-velocity relation in intact myosin filaments from skeletal and smooth muscles. *Am. J. Physiol. Cell Physiol.* **318**, C103-C110 (2020).
34. Caruel, M. & Truskinovsky, L. Physics of muscle contraction. *Rep. Prog. Phys.* **81**, 036602 (2018).
35. Joanny, J.-F., Kruse, K., Prost, J. & Ramaswamy, S. The actin cortex as an active wetting layer. *Eur. Phys. J. E.* **36**, 1–6 (2013).
36. Guo, B. & Guilford, W. H. Mechanics of actomyosin bonds in different nucleotide states are tuned to muscle contraction. *Proc. Natl. Acad. Sci. U. S. A.* **103**, 9844–9849 (2006).
37. Khoury, L. R., Nowitzke, J., Shmilovich, K. & Popa, I. Study of biomechanical properties of protein-based hydrogels using force-clamp rheometry. *Macromolecules* **51**, 1441–1452 (2018).
38. Weirich, K. L., Stam, S., Munro, E. & Gardel, M. L. Actin bundle architecture and mechanics regulate myosin II force generation. *Biophys. J.* (2021).
39. Courson, D. S. & Rock, R. S. Actin cross-link assembly and disassembly mechanics for α -actinin and fascin. *J. Biol. Chem.* **285**, 26350–26357 (2010).
40. Pollard, T. D. & Borisy, G. G. Cellular motility driven by assembly and disassembly of actin filaments. *Cell* **112**, 453–465 (2003).
41. Kotila, T. *et al.* Mechanism of synergistic actin filament pointed end depolymerization by cyclase-associated protein and cofilin. *Nat. Commun.* **10**, 1–14 (2019).
42. Bayley, H., Cazimoglu, I. & Hoskin, C. E. Synthetic tissues. *Emerg. Top. Life Sci.* **3**, 615–622 (2019).
43. Chan, V., Asada, H. H. & Bashir, R. Utilization and control of bioactuators across multiple length scales. *Lab Chip* **14**, 653–670 (2014).
44. Vogel, S. K., in *Cytoskeleton Methods and Protocols* (Springer, 2016), pp. 213–223.
45. Smith, D., Ziebert, F., Humphrey, D., Duggan, C., Steinbeck, M., Zimmermann, W., Käs, J., Molecular motor-induced instabilities and cross linkers determine biopolymer organization. *Biophys. J.* **93**, 4445–4452 (2007)
46. Conibear P. B., Bagshaw C. R.. Myosin monomer density and exchange in synthetic thick filaments investigated using fluorescence microscopy with single molecule sensitivity. *Proc. R. Soc. B*, 267(1441): 415–421(2000).

Materials And Methods

Preparation of BSA Solution

3.8 g bovine serum albumin (BSA) (Sigma Aldrich) and 1 mol% Biotinylated-BSA (ThermoFisher) and 1.62 mL of DMSO (18 v/v%) were added to 20 mM HEPES buffer to make up a total volume of 9 mL solution. The mixture was centrifuged (20000g) for 15 min to remove impurities and foam before use. 85 mM rose bengal (Sigma Aldrich, 330000) was prepared separately. The BSA photoresist (380 g/L) was prepared by mixing BSA resin and rose bengal at the ratio of 9:1 v/v.

3D BSA hydrogel printing

3D BSA hydrogel printing was processed with the Nanoscribe Photonic Professional (Nanoscribe GmbH). 3D structures were designed (Supplementary Fig. S2) and optimized (Supplementary Fig. S8) with Solidworks. The printing parameters were defined with Describe (Nanoscribe GmbH). The following printing parameters were used (Fig. 2c-d and g-h, Fig. 3b-c, Fig. 4; Extended Data Fig. 1, 3-5, and 7-10; Movie S2-5 and 7-8), laser power: 35 mW (70 %), scan speed: 30000 $\mu\text{m/s}$, slicing distance: 0.3 μm , hatching distance: 0.2 μm . All structures were printed with 63x NA1.4 objective in silicone isolator chambers (Round, 9 mm diameter, 1 mm depth, Thermo Fisher Scientific) pasted on round glass coverslips (Thermo Fisher, Diameter=30 mm, thickness #1.5). During printing, the chambers were covered with small coverslips to avoid strong evaporation. After fabrication, structures were rinsed with Phosphate Buffered Saline (PBS) buffer (pH 7) to remove the excess BSA resin and photoresist. PBS (pH 7) buffer was then used to store the structures and was further exchanged to other buffer solutions according to the experimental requirements. All the experiments, except for Scanning Electron Microscopy (SEM) imaging, should be performed in buffer solutions to maintain proper hydration of protein hydrogel. Biotinylation of structures was achieved using BSA doped with BSA-biotin for printing. As a consequence, our structures displayed free biotin groups exposed at the surface.

Young's modulus measurement with Atomic Force Microscopy (AFM)

AFM was performed on a JPK Instruments Nanowizard III BioAFM mounted on a Zeiss LSM510 Meta laser scanning confocal microscope (Jena, Germany). Silicon nitride cantilevers (XNC12/CR-AU B, MikroMasch), with typical spring constant of 0.32 N/m, were used for force spectroscopy and quantitative imaging (QI) modes. For typical measurements, the setpoint force was set to 2 nN, acquisition speed to 250 $\mu\text{m/s}$ and Z-length to 4 μm . Young's modulus of the microstructure was measured in solution containing 50 mM KCl, 2 mM MgCl_2 , 10 mM Tris-HCl (pH 7.5). Data was analyzed using JPK data processing software Version 5.1.4 (JPK Instruments). Young's modulus was obtained by fitting the extended part of the force-penetration curves ($n=900$) with a simple Hertz/Sneddon model, considering a quadratic pyramid tip shape and tip angle of 35 deg (using the JPK data analysis software).

Scanning Electron Microscopy (SEM) imaging of hydrogel

To prepare samples for SEM imaging, BSA microstructures were exchanged into acetone sequentially with increasing serial concentrations of acetone (20 %, 40 %, 60 %, and 100 %). The samples were then dried with Leica EM CPD300 Automated Critical Point Dryer after immersing in pure acetone. Samples

were sputter-coated with platinum/palladium on a high-resolution automatic sputter coater (Cressington 208HR) at 20 mA and 0.1 mbar Argon for 3×20 s. The thickness of the applied coatings was measured with a built-in thickness controller to be 2.0 nm. Coated surfaces were viewed using a TESCAN MIRA3 FESEM operating at an accelerating voltage of 10 kV in SE mode.

F-actin preparation

Actin filaments were prepared according to a previously published protocol⁴⁴. Briefly, 32 μL rabbit skeletal muscle actin monomers (Stock: 2 mg/mL, Molecular Probes) and 1.6 μL biotinylated rabbit actin monomers (Stock: 10 mg/mL, tebu-bio [Cytoskeleton Inc.]) were mixed in a 5:1 (actin:biotin-actin) ratio for a final concentration of 39.6 μM . Polymerization of the mixture (39.6 μM) was induced in F-Buffer containing 50 mM KCl, 2 mM MgCl_2 , 1 mM DTT, 1 mM ATP, 10 mM Tris-HCl buffer (pH 7.5). The biotinylated actin filaments were labeled and stabilized with 3.96 μM Alexa-Fluor 647 Phalloidin (Stock: 6.6 μM , Molecular Probes) according to the manufacturer's protocol. An actin-stabilizing solution was prepared by placing 60 μL of 6.6 μM Alexa Fluor 647 phalloidin in a 1.5 mL Eppendorf tube and dried in a vacuum centrifuge at room temperature. The dried powder was dissolved in 5 μL methanol and further diluted with 85 μL labeling buffer. The labeling buffer contains 10 mM 3-(N-morpholino)propanesulfonic acid (MOPS, pH 7.0), 0.1 mM ethylene glycol-bis(β -aminoethyl ether)-N,N,N',N'-tetraacetic acid (EGTA) and 3 mM NaN_3 . Then, 39.6 μM actin was diluted with the labeling buffer to 20 μM actin. 10 μL of 20 μM actin was further diluted with 90 μL actin-stabilizing solution to obtain 2 μM (refers to monomers) of Alexa-647-Phalloidin labeled biotinylated actin filaments.

Myofilaments preparation

Myosin (21 μM stock solution) was purified from rabbit skeletal muscle tissue as previously described⁴⁵. 0.3 μM myofilament assembly (refer to the monomers) was induced in reaction buffer containing 50 mM KCl, 2 mM MgCl_2 , 1 mM DTT and 10 mM Tris-HCl buffer (pH 7.5). Equilibration of the mixture for approximately 30 min gave us a median length of 560 nm in our system²⁶.

Myosins were labeled with thiol-reactive dyes AlexaFluor 488 maleimide (Molecular Probes) in a slight variation according to published protocol²⁶. In brief, the thiol-reactive dyes were dissolved in DMSO to 10 mM concentration. The myosin stock was diluted to 2 μM in reaction buffer containing 300 mM KCl, 10 mM Tris-HCl buffer (pH 7.5) and 2 mM MgCl_2 . The solution was deoxygenated for 15 min under vacuum and put into N_2 environment. 15 times molar excess (30 μM) of TCEP (tris(2-carboxyethyl)phosphine, Molecular Probes) was added to the solution and incubated for 1 hour at room temperature. 25-fold molar excess to reach 50 μM of the maleimide dyes were added dropwise to the solution while it was stirred and incubated overnight at 4 °C. Labeled myosin monomers were purified from the remaining dyes by gel filtration with the Sephadex G-25 Column (GE Healthcare) according to the manufacturer protocol. 300 mM KCl and 10 mM Tris-HCl buffer (pH 7.5) was used as elution buffer. The fractions were measured with plate reader Infinite 200 PRO (Tecan) and the fraction with the highest signal was used.

Aliquots were frozen and stored at $-80\text{ }^{\circ}\text{C}$ with 50 % glycerol. 10 % labeled myosin was used for the actin-myosin network imaging.

Active contraction on 3D printed hydrogel structures

Biotinylated 3D hydrogel structures were transferred from PBS to the buffer containing 50 mM KCl, 2 mM MgCl_2 , 10 mM Tris-HCl (pH 7.5) by buffer exchanging and further incubated with 10 $\mu\text{g}/\text{mL}$ neutravidin (Stock: 1 mg/mL) for at least half an hour. Then the free neutravidin was gently washed away with washing buffer containing 50 mM KCl, 2 mM MgCl_2 , 10 mM Tris-HCl (pH 7.5). The microstructures were further incubated with 0.3 μM (refer to the monomer concentrations) pre-formed actin filaments and 2.25 nM neutravidin (neutravidin: biotin-actin, 1:20) for 2 h, followed by carefully washing with buffer. For active contraction, 0.5 mM ATP was added to 100 μL pre-formed myofilaments first and then this solution was further added into the reaction chamber containing 60 μL buffer solution (Fig. 2, Fig. 3b, Fig. 4a-g, Extended Data Fig. 1-9, and Movie S1-7). The imaging was done immediately after adding myofilaments.

Reversibility of the microstructures was conferred by adding 4 mM ATP after the hydrogel structures were deformed (Fig. 3c-d). Recovery of the contraction could be obtained by gently washing away the high concentration ATP, and then the buffer condition was exchanged to 0.5 mM ATP. All the steps were controlled manually by pipetting, the shear force and dilution effect of which may limit the full mechanical reversibility. Therefore, all the washing steps should be processed gently. Since the reversible structure has a round joint (Supplement Fig. S2c), the distances between the tips of the two arms were used to quantify the dynamics of reversibility.

Photoactivation: 1 mM NPE-caged-ATP (Adenosine-5'-triphosphate, P3-(1-(2-nitrophenyl)-ethyl)-ester, Jena Bioscience) was used instead of the normal ATP for supplying the energy for the pre-formed myofilaments (Fig. 4i and Extended Data Fig. 10). Actin network coated microstructures were incubated with 100 μL 0.3 μM pre-formed myofilaments and 1 mM NPE-ATP for 0.5-1.5 h, and then imaged in darkness by the confocal microscope. The photocleavage was induced by illumination with 405 nm laser diode (30 mW). The spatial photoactivation was controlled with the photobleaching mode of the LSM 780 confocal microscope. The photoactivation time was controlled by the number of bleaching iterations.

Myofilaments quantification

The numbers of myofilaments in the actin network were estimated through quantitative fluorescence microscopy. First, 1 μM AlexaFluor-488 labeled myosin monomers (labeling efficiency: 1.3) were diluted to various concentrations (0.001-1 μM). The serial dilutions were processed in the protein LoBind® Tubes (Eppendorf) and then were transferred to the PLL-PEG- passivated microwell plate. The fluorescence intensity (mean) was measured by using the same microscope and camera settings as the actomyosin gel measurement (Microscope: LSM800; objective: C-Apochromat 40x/1.2 W Korr, Laser power: 1 %; detection wavelength: 410-546 nm; gain: 700 V; scaling per pixel: 0.099x0.099 μm). For fluorescence intensity measurements, the microscope was focused on the solution that is far away from the chamber

surface where intensity was maximal, and images were taken at different areas ($n > 4$). The fluorescence signals were plotted against the myosin concentrations. Then the averaged local concentration of the labeled myosin was calculated in accordance with the standard curve. The myofilaments number was further calculated according to the labeling ratio (10 %), local volume (inner: $1055 \mu\text{m}^3$; ring: $1225 \mu\text{m}^3$), average myosin monomer density on myofilaments ($560 \text{ molecules}/\mu\text{m}^4$) and the averaged myofilament length ($0.56 \mu\text{m}^{26}$). The calculations were repeated with nine independent experiments.

Image analysis and reproducibility of experiments.

Image analysis and processing was carried out with Fiji and ZEN Software. Representative micrographs and intensity curves correspond to at least four successfully repeated experiments. The number of replicated experiments is given in the respective figure captions. For generating actin network heatmaps, actin networks on pillar rings were imaged in the same experimental session using the same microscope and camera settings. The actin networks were prepared according to the above method section and imaged after two hours' incubation. Z-stacks of actin networks were projected with maximum intensity separately. Then the network patterns from eight replicate experiments were incorporated into a z-stack by importing the z-projection images as a sequence. The images in the z-stack were further aligned in Fiji with the plugin "MultiStackReg" (Transformation: rigid body) and were projected (Z-projection) with average intensity. A 16 colors lookup was chosen for the heatmap generation (Fluorescence calibration range, Min-Max: 0-50000).

Force quantification.

The deflection profiles were extracted from the confocal microscopy images of the deformed pillars with Fiji. To this end, the data was first binarized. For a better separation of adjacent pillars, the build-in watershed algorithm was used. The images could then be analyzed with the help of Fiji's particle analysis tool, which tracked the cross area of the pillars and calculated the position of the 'center of mass' for each slice of the pillar. To obtain an estimate of the force, generated by the actomyosin gel, the pillar profile was predicted from elasticity theory (Supplementary Text, SI-Sec. 1). Subsequently, a one-parameter fit was performed to obtain the force. For the fit, the data from a height below $2 \mu\text{m}$ is ignored, since the pillar has a stiffer foot, which is hardly deflected. Note that the pillars are not always perfectly straight before they are deformed by the myosin activity. To exclude this effect from the analysis, we correct the observed final deflection by subtracting the fitted initial profile. The diameters and heights of the pillars were measured with SEM and confocal imaging. The codes for force calculation are available upon request.

Figures

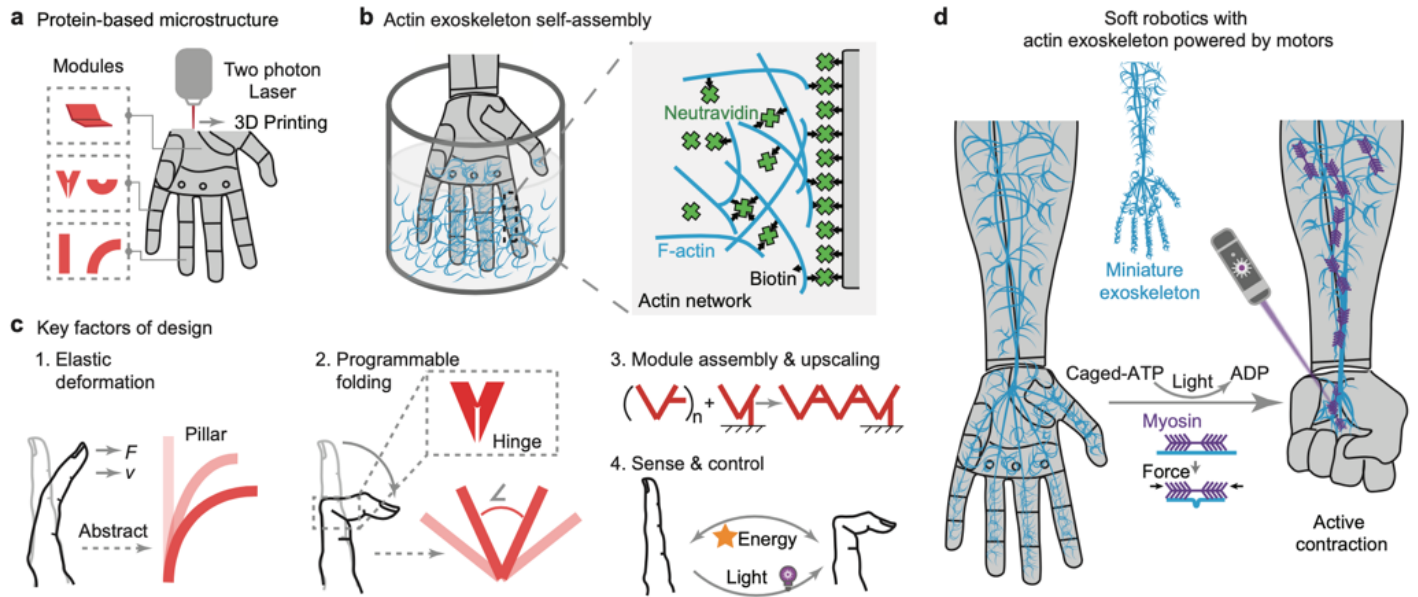


Figure 1

Key design concepts of protein-based soft robotic structures with an exoskeleton powered by molecular motors. a.) 3D protein hydrogel printing procedure and b.) Coupling of an actomyosin exoskeleton to the scaffold. c.) Bioinspired design modules to program and upscale the protein-based soft robotics. d.) Soft robotic arm powered by light-targeted molecular motor activity on the miniature exoskeleton.

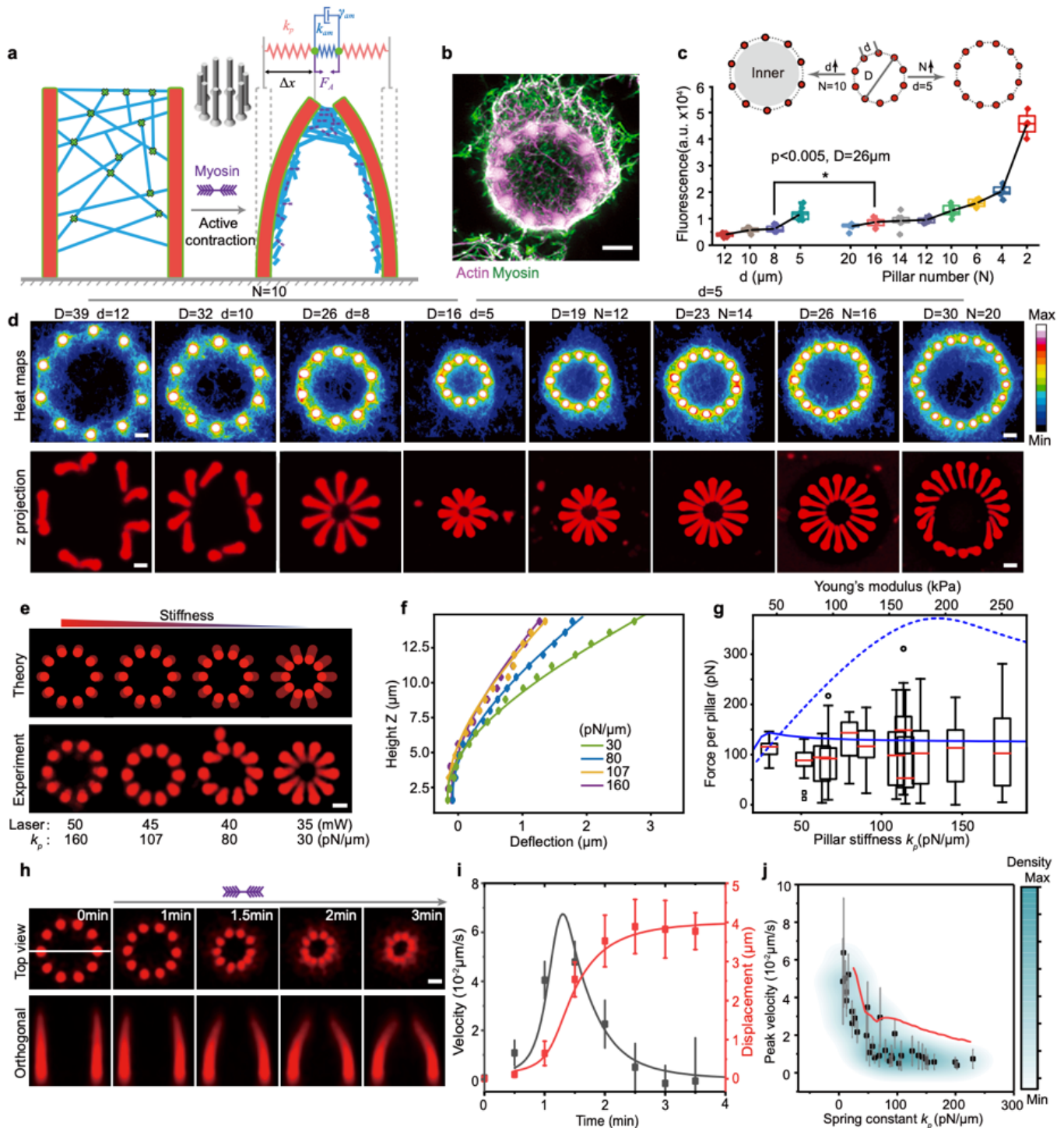


Figure 2

Pillar-based model system to quantify force production by contractile cortices on BSA hydrogel structures. a.) Scheme depicting the coupling of an actomyosin exoskeleton to 3D printed protein hydrogel pillars. b.) Z-projection of actomyosin exoskeleton on a pillar ring, scale bar 5 μm . c.) Fluorescence intensity of Alexa-647-Phalloidin labeled actin network on the pillar rings with different diameters (D , μm) and pillar distances (d , μm). The intensities were averaged for the inner ring areas shown with grey background in the scheme ($n=8$). *Analysis of Variance (ANOVA) one-way statistical test. d.) Fluorescence heatmaps of actin networks on pillar rings with different sizes and pillar distances.

Z-projections illustrate the contracted state of pillar rings. Scale bar, 5 μm . The heatmaps demonstrate the averaged fluorescence intensity maps of actin networks imaged with confocal microscopy ($n=8$). The Min/Max of color bar levels the same for all images. e.) Theoretical and measured (z-projection) contraction for pillar rings with different stiffness. Scale bar, 5 μm . For the predicted pillar profiles, the force measured for the stiffest pillar was used ($F_A=115$ "pN"). f.) Experimentally measured deflection (diamonds) and theoretical fits (lines) for pillars with different stiffness (same stiffnesses as in e.). g.) Active force per pillar exerted on the pillar ring with different stiffnesses ($n=10$). Blue lines represent theoretical prediction of the generated active force with a purely density-dependent contractility (dashed) and with myosin binding contractility model (solid). h.) Contractile dynamics of the pillar ring in response to motor activation. Scale bar, 5 μm . i.) Pillar tip displacement and velocity during contraction ($k_p=35$ "pN/ μm "): experimental data (points), fit by myosin binding contractility model (solid lines). j.) Maximal velocity vs. pillar spring constant. Data are shown as mean \pm s.d.; $n = 10$ pillars analyzed for each data point. The solid red line represents the theoretical prediction. Box plots in c and f: lines are median, box limits are quartiles 1 and 3, whiskers are $1.5 \times$ interquartile range and points are outliers. Active contractions in Fig. 2 were initiated with 0.5 mM ATP. Red fluorescence in d. e. and g. result from the hydrogel itself, while the reconstituted actomyosin networks are not shown in the figure.

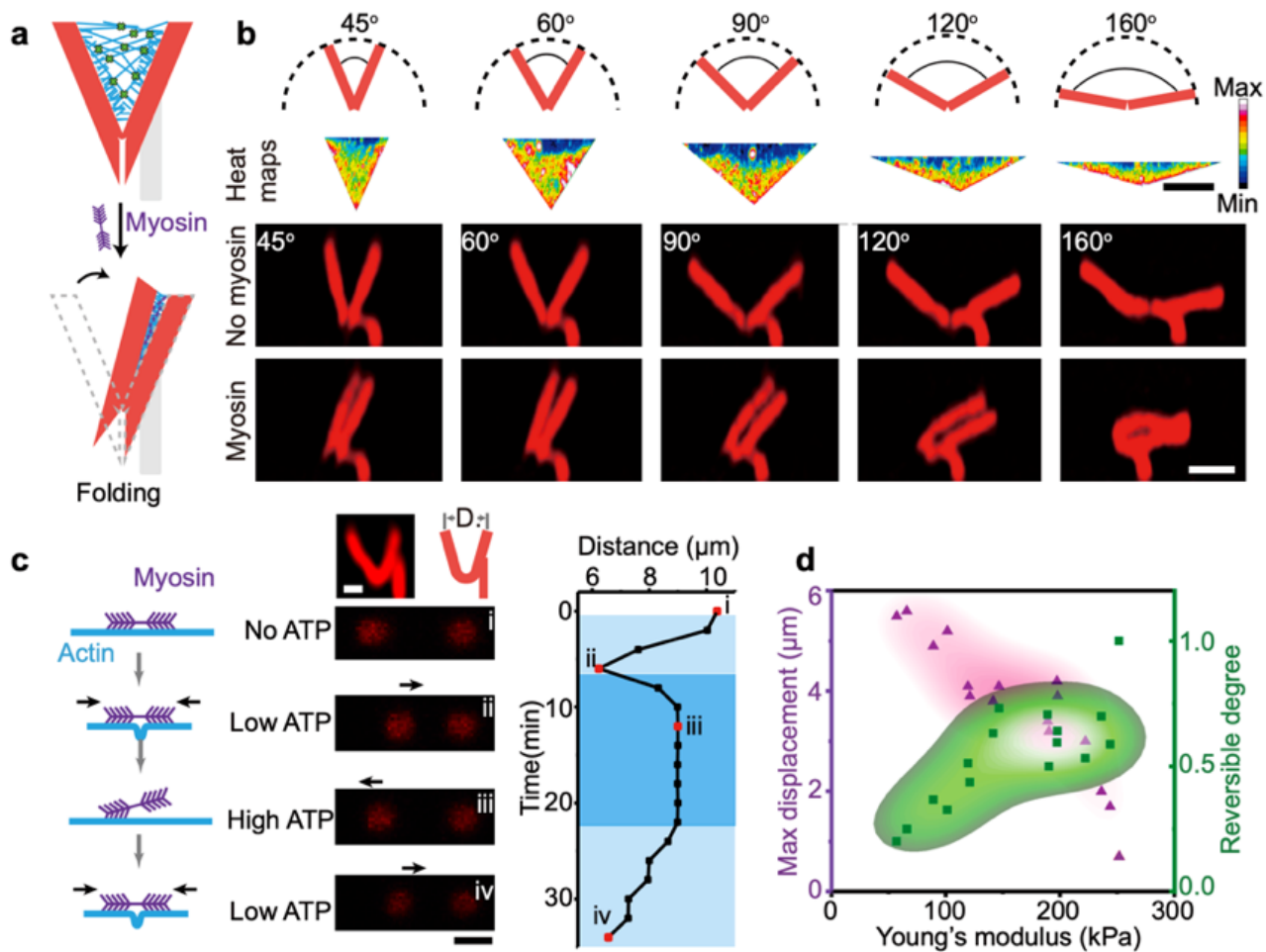


Figure 3

Reversible operation of hinged 3D V-units by switching ATP concentrations. a.) Schematics of free-standing V-units and b.) active folding of V-units with different opening angles (0.5mM ATP). Heatmaps: Density of actin-myosin network on V-units (n=8). Scale bar, 10 μm . c.) Reversibility of V-units with round joints in response to different ATP concentrations (0.5mM and 4mM ATP). Scale bar, 5 μm . Images show V-units viewed from the side and above. The plot describes the reversible opening and closure. d.) Density maps of maximal displacement and reversibility versus Young's modulus. Degree of reversibility was determined from the distances between reversed and contracted state. The density map is based on data points that were measured in independent experiments. The reconstituted actin and myosin networks are not shown in this figure.

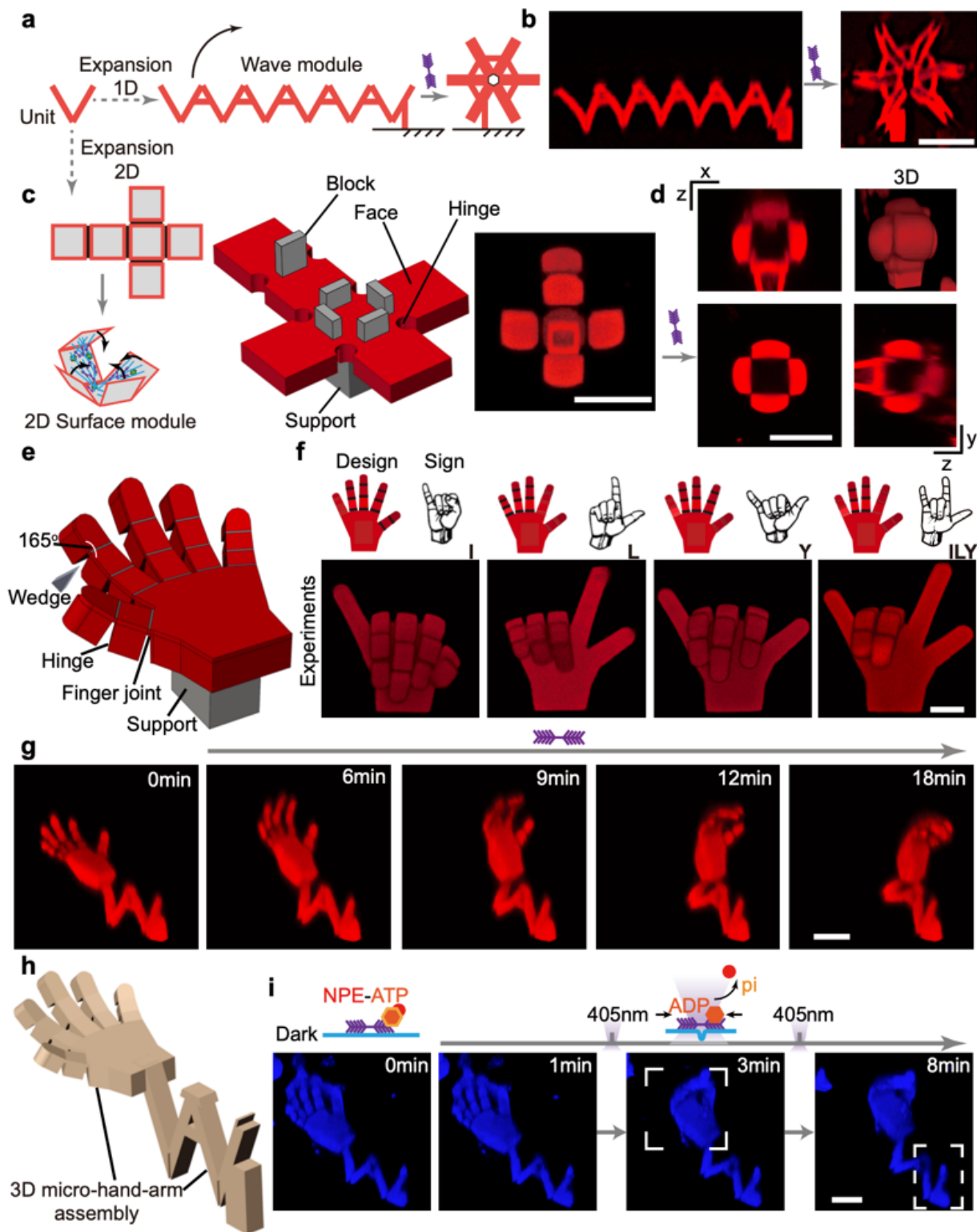


Figure 4

Large-scale transformations of complex 3D structures by targeted biomimetic actuation. a.) Schematic design and b.) experimental data of concatenated V-units demonstrating complex coiling dynamics upon exoskeleton actuation. Scale bar, 20 μm . c-d.) Cubic box actively self-folding from cruciform precursor. Orthogonal view and 3D imaging demonstrate cube closure upon chemical energy addition (0.5mM ATP). Scale bar, 20 μm . e-i.) Design and spatiotemporal control of biomimetic 4D soft robotics. e.) Design and

f.) experimental results of microhands showing different gestures. Scale bar, 10 μm . The gestures are from different designs according to American Sign Language. To program the hand gestures, the hinges are selectively designed with triangular-shaped blocker modules (wedges). These wedges can increase the stiffness of the joint and constrain involuntary movement. g-h.) Dynamic actions of the robotic arm. Scale bar, 10 μm . i.) Spatiotemporally induced sequential actuation of a modular robotic arm by light (1 mM NPE-caged-ATP). Scale bar, 10 μm . Blue signals in h. are from Alexa-647-Phalloidin labeled actin. The reconstituted actin-myosin networks are not shown in a-g. Active contractions in b-g were initiated with 0.5 mM ATP.

Supplementary Files

This is a list of supplementary files associated with this preprint. Click to download.

- [MovieS1.mp4](#)
- [MovieS2.avi](#)
- [MovieS3.mp4](#)
- [MovieS4.avi](#)
- [MovieS5.avi](#)
- [MovieS6.avi](#)
- [MovieS7.avi](#)
- [MovieS8.avi](#)
- [ExtendedDataFig.11.pdf](#)
- [ExtendedDataFig.21.pdf](#)
- [ExtendedDataFig.31.pdf](#)
- [ExtendedDataFig.41.pdf](#)
- [ExtendedDataFig.51.pdf](#)
- [ExtendedDataFig.61.pdf](#)
- [ExtendedDataFig.71.pdf](#)
- [ExtendedDataFig.81v2.pdf](#)
- [ExtendedDataFig.91.pdf](#)
- [ExtendedDataFig.101v2.pdf](#)
- [ExtendedDatafigurecaptions.docx](#)
- [JlaetalSIrevision2.docx](#)